



## **The magnetic field of the Radcliffe wave: Starlight polarization at the nearest approach to the Sun**

Downloaded from: <https://research.chalmers.se>, 2025-04-03 05:10 UTC

Citation for the original published paper (version of record):

Panopoulou, G., Zucker, C., Clemens, D. et al (2025). The magnetic field of the Radcliffe wave: Starlight polarization at the nearest approach to the Sun. *Astronomy and Astrophysics*, 694. <http://dx.doi.org/10.1051/0004-6361/202450991>

N.B. When citing this work, cite the original published paper.

# The magnetic field of the Radcliffe wave: Starlight polarization at the nearest approach to the Sun

G. V. Panopoulou<sup>1,\*</sup>, C. Zucker<sup>2</sup>, D. Clemens<sup>3</sup>, V. Pelgrims<sup>4</sup>, J. D. Soler<sup>5</sup>, S. E. Clark<sup>6,7</sup>,  
J. Alves<sup>8</sup>, A. Goodman<sup>2</sup>, and J. Becker Tjus<sup>1,9,10</sup>

<sup>1</sup> Department of Space, Earth and Environment, Chalmers University of Technology, Gothenburg, Sweden

<sup>2</sup> Center for Astrophysics | Harvard & Smithsonian, 60 Garden St., Cambridge, MA 02138, USA

<sup>3</sup> Institute for Astrophysical Research, Boston University, 725 Commonwealth Avenue, Boston, MA 02215, USA

<sup>4</sup> Université Libre de Bruxelles, Science Faculty CP230, 1050 Brussels, Belgium

<sup>5</sup> Istituto di Astrofisica e Planetologia Spaziali (IAPS), INAF, Via Fosso del Cavaliere 100, 00133 Roma, Italy

<sup>6</sup> Department of Physics, Stanford University, Stanford, CA 94305, USA

<sup>7</sup> Kavli Institute for Particle Astrophysics & Cosmology, Stanford University, PO Box 2450, Stanford, CA 94305, USA

<sup>8</sup> University of Vienna, Department of Astrophysics, Türkenschanzstrasse 17, 1180 Vienna, Austria

<sup>9</sup> Theoretische Physik IV, Fakultät für Physik & Astronomie, Ruhr-Universität Bochum, 44780 Bochum, Germany

<sup>10</sup> Ruhr Astroparticle and Plasma Physics Center (RAPP Center), Ruhr-Universität Bochum, 44780 Bochum, Germany

Received 4 June 2024 / Accepted 5 December 2024

## ABSTRACT

**Aims.** We investigate the geometry of the magnetic field toward the Radcliffe wave, a coherent part of the nearby Local Arm of 3 kpc in length recently discovered via three-dimensional dust mapping.

**Methods.** We used archival stellar polarization in the optical and new measurements in the near-infrared to trace the magnetic field as projected on the plane of the sky. Our new observations cover the portion of the structure that is closest to the Sun, between Galactic longitudes of 122° and 188°.

**Results.** The polarization angles of stars immediately behind the Radcliffe wave appear to be aligned with the structure as projected on the plane of the sky. The observed magnetic field configuration is inclined with respect to the Galactic disk at an angle of 18°. This departure from a geometry parallel to the plane of the Galaxy is contrary to previous constraints from more distant stars and polarized dust emission. We confirm that the polarization angle of stars at larger distances shows a mean orientation parallel to the Galactic disk.

**Conclusions.** We discuss the implications of the observed morphology of the magnetic field for models of the large-scale Galactic magnetic field, as well as formation scenarios for the Radcliffe wave itself.

**Key words.** techniques: polarimetric – dust, extinction – ISM: magnetic fields – ISM: structure – local interstellar matter

## 1. Introduction

The magnetic field is one of the most elusive components of the Milky Way, mainly because of the difficulties associated with measuring it (Beck & Wielebinski 2013; Haverkorn 2015; Han 2017). Our understanding of the magnetic field is markedly improving, partly due to the advent of the *Planck* mission (Planck Collaboration I 2011). Observations of the polarization of thermal dust emission have revealed the morphology of the magnetic field in the dusty interstellar medium (ISM) with unprecedented sky coverage (Planck Collaboration XII 2020).

On scales of hundreds of parsecs to roughly one kiloparsec, the *Planck* data in the Galactic plane trace a magnetic field that is parallel to the disk (Planck Collaboration Int. XIX 2015; Planck Collaboration Int. XXI 2015), confirming what had been known from starlight polarization (Mathewson & Ford 1970; Heiles 2000; Fosalba et al. 2002). However, new results from the Galactic Plane Infrared Polarization Survey (GPIPS; Clemens et al. 2020) find significant variations among the polarization angles of stars, with regions showing departures from the disk orientation within the inner Galaxy. It remains unclear what physical scales these variations of the cumulative polarization of

stars are probing, potentially arising, for example, from the presence of dense molecular clouds. On scales of tens of parsecs, the magnetic field orientation can vary substantially from the disk geometry when probing dense clouds (e.g., Stephens et al. 2011; Marchwinski et al. 2012; Planck Collaboration Int. XXXV 2016). On such scales, the *Planck* data show that the magnetic field orientation is correlated with that of dust structures (Planck Collaboration Int. XXXII 2016) and linear features in the neutral atomic hydrogen (HI) emission throughout the sky (Clark et al. 2014, 2015). The origin of this correlation has been connected to the properties of magnetohydrodynamic (MHD) turbulence (e.g., Soler & Hennebelle 2017; Xu et al. 2019). However further observational evidence is needed to fully understand the coupling of the magnetic field and density across scales (e.g., Clark et al. 2019; Hennebelle & Inutsuka 2019).

These advances in mapping the magnetic field have coincided with significant improvements in our ability to reconstruct the three-dimensional (3D) distribution of dust (cf. Green et al. 2019, Lallement et al. 2022, Edenhofer et al. 2024), thanks to the advent of the *Gaia* mission (Gaia Collaboration 2016). These 3D dust maps are transforming our view of the ISM structure within a few kiloparsecs from the Sun, revealing new and unexpected structures in the 3D density distribution (Zucker et al. 2023). One of the most striking new discoveries is the Radcliffe

\* Corresponding author; [georgia.panopoulou@chalmers.se](mailto:georgia.panopoulou@chalmers.se)

wave (RW), a structure 2.7 kpc in length with an aspect ratio of roughly 20 : 1, which also hosts many nearby star-forming regions (Alves et al. 2020).

The RW seems to be a prominent feature of Galactic structure, argued (e.g., Swiggum et al. 2022) to be the gaseous reservoir of the Local Arm (Reid et al. 2019) in the solar vicinity. It exhibits the puzzling shape of a damped sinusoid extending above and below the midplane of the Galaxy with an amplitude of roughly 160 pc and crossing the midplane near Galactic longitude  $l = 165^\circ$ . Despite its prominence, there are important open questions regarding its origin and role in the history of the local ISM. It is possible that the wave was caused by a perturber that collided with the disk (Thulasidharan et al. 2022), though internal mechanisms, including a series of supernova explosions that displaced the gas from the midplane, are also possible (Tu et al. 2022). Using new constraints on the 3D space motions of young stellar clusters detected in the wave with Gaia DR3, Konietzka et al. (2024) show that the structure is oscillating with a maximum vertical velocity (perpendicular to the disk of the Milky Way) of  $v_z \approx 14 \text{ km s}^{-1}$  (see also Li & Chen 2022).

The existence of this feature is perplexing in terms of our understanding of the Galactic magnetic field (GMF). Measurements of stellar polarization have been used to determine the mean direction of the magnetic field in the Local Arm (Heiles 1996), finding that the field runs parallel to the Galactic plane. At the same time, the RW is part of the Galactic disk but does not lie parallel to the disk: it appears to undulate above and below the disk. This apparent discrepancy between the orientation of the magnetic field and the shape of the RW calls for a detailed investigation.

For this paper we performed a study of the magnetic field toward the RW. Our aim was to trace the Galactic magnetic field in the vicinity of the RW and determine whether it has been affected by the presence of the RW. We used starlight polarization in combination with stellar distances to probe the magnetic field morphology at the distance to the RW. Section 2 presents the data used in this study. Section 3 describes the statistical treatment of the stellar polarization data. Section 4 compares the magnetic field geometry as traced by stellar polarimetry to the morphology of the RW, and shows that within 400 pc of the Sun, the mean magnetic field is preferentially aligned with the RW and not with the Galactic plane at longitudes  $l = 122\text{--}188^\circ$ . Our findings are discussed in Sect. 5, and our conclusions are provided in Sect. 6.

## 2. Data

### 2.1. 3D dust extinction map

We used the publicly available 3D dust extinction map from Edenhofer et al. (2024) to trace the distribution of dust toward the RW. The map was constructed using 54 million stars from Zhang et al. (2023), who forward-modeled the stars' atmospheric parameters, distances, and extinctions using the low-resolution Gaia BP/RP spectra (Carrasco et al. 2021). We chose the Edenhofer et al. (2024) map because it achieves good spatial resolution both on the plane of sky (POS) and along the line of sight (LOS), with  $14'$  angular resolution and parsec-scale distance resolution. The Edenhofer et al. (2024) map extends out to 1.25 kpc from the Sun, which encompasses the bulk of the RW. We used the publicly available version of the map<sup>1</sup> provided in HEALPix format (Górski et al. 2005). This is a collection of 516

HEALPix maps of  $N_{\text{side}} = 256$ , each corresponding to a different logarithmically spaced distance bin along the LOS, spanning distances from 69 to 1244 pc. We used the mean value in each pixel, which is given in arbitrary units of differential extinction. Following the recommendation from Edenhofer et al. (2024), we multiplied the values of the map by 2.8 to obtain  $A_V$  in magnitudes, based on the published extinction curve from Zhang et al. (2023).

### 2.2. Radcliffe wave model

Alves et al. (2020) constrain the “spine” of the RW in Heliocentric Galactic cartesian space by fitting a damped sinusoidal model to the 3D distribution of nearby molecular clouds from Zucker et al. (2020). Their model for the RW spine was obtained using a dynamic nested sampling package for estimating Bayesian posteriors and evidences (Speagle 2020). We used their best-fit model<sup>2</sup> as our default model, and also used 20 samples drawn from the posterior distribution of the solution to investigate the dependence of our results on the choice of model. We refer to the 20 samples as ‘alternative’ models in the rest of the text. We converted each RW spine model to a spherical coordinate system of longitude, latitude, and distance ( $l, b, d$ ) to compare with the polarization measurements both on the plane of the sky and along the LOS.

Figure 1 shows the default model of the RW spine as projected on the sky. Points on the spine are colored according to their distance from the Sun. The background shows the  $A_V$  map from Edenhofer et al. (2024), integrated out to a maximum distance of 1.25 kpc. The model extends over a large range of longitudes:  $l = (78^\circ, 224^\circ)$  and intersects the midplane ( $b = 0^\circ$ ) at  $l = 164^\circ$ . The 20 alternative models are also shown as white dotted curves. They span a range of locations and shapes.

#### 2.2.1. Polarized dust emission from *Planck*

We used the *Planck* 353 GHz maps of Stokes  $Q$  and  $U$  to study the polarization angles of dust emission in the sky region containing the RW. We selected the  $80'$ -resolution maps produced via the Generalized Needlet Internal Linear Combination (GNILC) algorithm (Remazeilles et al. 2011), which reduces the contamination from the Cosmic Microwave Background (CMB) and instrumental noise in polarization (Planck Collaboration IV 2020). We smoothed the Stokes  $Q$  and  $U$  maps and their covariance matrices to a FWHM =  $2^\circ$  using the smoothing function of the healpy package and the procedure described in Appendix A of Planck Collaboration Int. XIX (2015).

The polarization angle of the dust emission in the Galactic reference frame according to the IAU convention is

$$\phi_{\text{dust}} = 0.5 \arctan(-U, Q), \quad (1)$$

where we have used the two-argument arctangent function. We rotated the angles by  $90^\circ$  to obtain the corresponding plane of sky magnetic field orientations,  $\theta_{\text{dust}}$ . The polarized intensity and its uncertainty were computed as

$$P = \sqrt{Q^2 + U^2}, \quad \sigma_P = 1/P \sqrt{Q^2 C_{QQ} + U^2 C_{UU}}, \quad (2)$$

where  $C_{QQ}, C_{UU}$  are the diagonal terms of the covariance matrix and we have ignored correlations between  $Q$  and  $U$  (see also

<sup>1</sup> <https://doi.org/10.5281/zenodo.8187943>

<sup>2</sup> <https://doi.org/10.7910/DVN/OE51SZ>

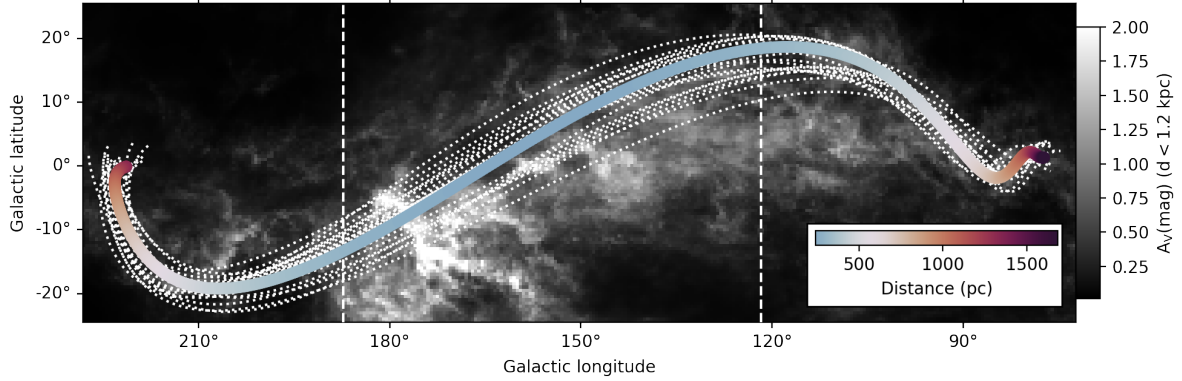


**Fig. 1.** Default model of the RW spine (thick colored line) as projected on the sky. The colors indicate the distance of the RW from the Sun at the corresponding point along the RW spine. The background image shows the extinction integrated out to 1.25 kpc from [Edenhofer et al. \(2024\)](#). The 20 alternative RW models are shown as dotted white lines. The dashed vertical white lines mark the span of the longitude range of interest.

equation B.4, [Planck Collaboration Int. XIX 2015](#)). We calculated the uncertainty in polarization angle as

$$\sigma_{\phi,dust} = 28.65^\circ \sigma_P / P, \quad (3)$$

which is a good estimator of the uncertainty at high S/N ([Naghizadeh-Khouei & Clarke 1993](#)).

### 2.3. Starlight polarization data

We used a combination of archival data and new, targeted observations to obtain a sample of stars with stellar polarization at known distances probing the RW. These datasets are described below.

#### 2.3.1. Compilation of optical polarization catalogs from the literature

We used the compilation of stellar polarization catalogs presented in [Panopoulou et al. \(2025\)](#) (hereafter P2025). This compilation combines optical polarimetry for  $\sim 55\,000$  stars from a large body of published literature. We used the data from their Table 5, which contains polarimetry and distances from *Gaia* EDR3 for  $\sim 42\,000$  stars. We removed sources flagged as intrinsically polarized. We also removed stars with unknown uncertainties in the polarization fraction and polarization angle, resulting in a catalog of 35 864 stars over the sky. We make further selections based on the stars' positional proximity to the RW in Sect. 3.

#### 2.3.2. New NIR polarization data from Mimir

We conducted a targeted survey of stellar polarization along the nearby portion of the RW using the Mimir near-infrared (NIR) polarimeter ([Clemens et al. 2007](#)). To ensure a measurable polarization signal, we selected fields with  $A_V > 1.4$  mag based on the 3D dust map of [Green et al. \(2019\)](#), integrated out to 350 pc (covering the nearest distance of the RW, see Fig. 2). While we used the [Edenhofer et al. \(2024\)](#) 3D dust map for the majority of the analysis, we originally chose the [Green et al. \(2019\)](#) for target selection, as it was the highest-angular resolution 3D dust map available in the literature at the time of observations. A similar 3D dust mapping methodology used by [Green et al. \(2019\)](#) was used in [Alves et al. \(2020\)](#) to originally detect the RW (see [Zucker et al. 2019](#); [Zucker et al. 2020](#)). The fields were selected to lie within  $\sim 5^\circ$  of the RW spine and in areas that did

not have existing stellar polarization measurements from the literature. By cross-matching the 2MASS catalog ([Skrutskie et al. 2006](#)) with *Gaia*, we further required the observed regions to have at least 4 stars each within the  $10' \times 10'$  field of view of Mimir, at distances  $d \leq 350$  pc and that were bright enough to have significant detection of the polarization (apparent H-band magnitude  $m_H < 13.5$  mag).

For each pointing, we rotated the half-wave plate to 16 different position angles, with fixed integration times for each position. Sky dithering was performed in six positions, with offsets of typically 15 arcsec. This resulted in  $6 \times 16 = 96$  images per observation. Following [Pavel \(2011\)](#), we observed each field using multiple exposures: a short exposure of 2.3 s and two long exposures of 15 s per image. Observations were conducted during January/February 2020 and January 2022. The final catalog of stellar polarizations contains measurements toward 19 fields across the length of the RW, within the longitude range  $l = [122^\circ, 188^\circ]$ .

The data reduction was done with the IDL software packages described in [Clemens et al. \(2012\)](#). The reduction was performed separately on each series of short and long exposures, producing three polarization catalogs. The catalogs contain information on the relative Stokes parameters  $q = Q/I$ ,  $u = U/I$  (where  $I$  is the total intensity of the star), their uncertainties, as well as stellar coordinates, star identifiers and photometry from 2MASS. These polarization catalogs for the short and two long exposures were merged by matching the common stars and computing the weighted average Stokes  $q$  and  $u$  parameters based on their corresponding uncertainties. The fractional linear polarization,  $p$ , and Electric Vector Position Angle (EVPA),  $\chi$ , are defined from the Stokes parameters as

$$p = \sqrt{q^2 + u^2}, \quad \chi = 0.5 \arctan(u, q), \quad (4)$$

where the two-argument arctangent function is used. In this work, we do not correct for bias in  $p$  ([Vaillancourt 2006](#)), as we are interested solely in the polarization angle (and its uncertainty).

We applied quality cuts on the output polarization catalog, keeping stars with H-band brightness  $m_H \leq 13$  mag and signal-to-noise ratio (S/N) in the biased polarization fraction of  $p/\sigma_p \geq 2$ . Stars not satisfying these criteria were rejected from the final catalog. In total 477 stars passed these selection criteria and were included in the final catalog.

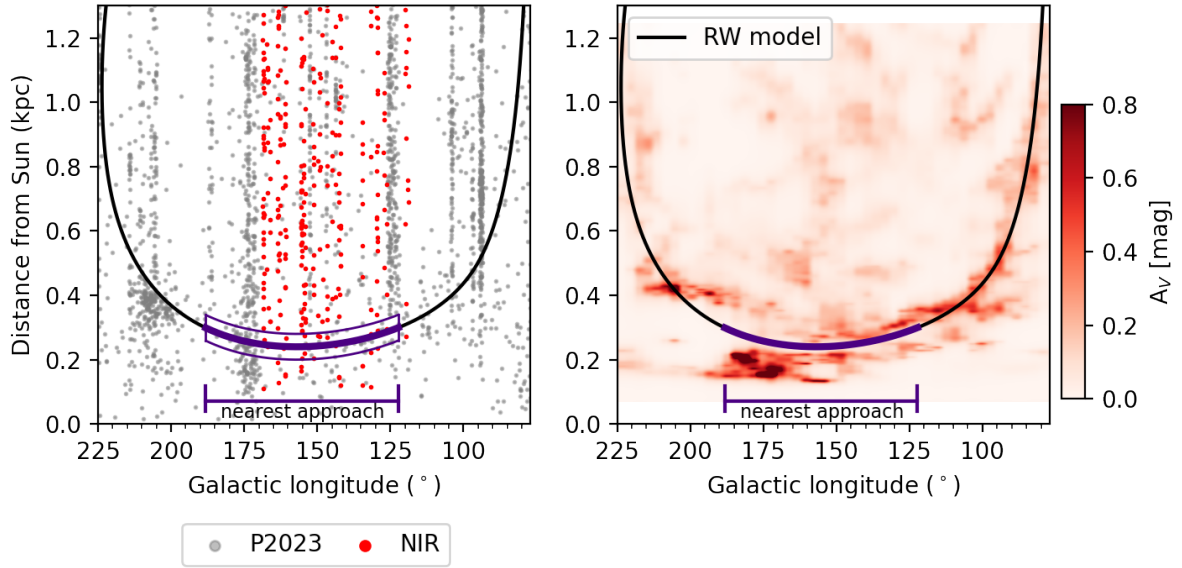


**Fig. 2.** Selection criteria in the distance-longitude diagram. Left: default RW spine model (black line) with nearest-approach longitude range marked in purple. The purple outline marks the part of the RW spine included in the nearest approach longitude range. Filled circles mark the positions of stars in the polarization catalogs we employ, namely the optical P2025 compilation (gray), and the two samples in the NIR from Mimir (red). Only stars with high-significance measurements of distance and polarization are shown. Right: extinction integrated along the latitude axis, from [Edenhofer et al. \(2024\)](#) for pixels within  $10^\circ$  of the default RW spine.

### 2.3.3. NIR polarization data of open clusters from Mimir

[Hoq & Clemens \(2015\)](#) and [Hoq \(2017\)](#) reported Mimir H-band polarimetry obtained toward fields containing 31 Open Clusters in the outer Milky Way. The data collection mode was similar to that described in Sect. 2.3.2, but with integration times chosen to match stellar brightnesses in each cluster. As such, the limiting magnitude varies for each observation. The 14 clusters, spanning  $\ell = 119^\circ$ – $168^\circ$ , which contributed data to this current study included Berkeley 12, Berkeley 14, Berkeley 18, Berkeley 60, Berkeley 70, King 1, King 5, King 7, NGC 559, NGC 663, NGC 869, NGC 1245, NGC 1857 and NGC 2126. The dates of observations range from January 2006 to January 2013. The limiting polarimetric magnitude, which accounts for 90% of all stars brighter than that value, ranges from 11.1 to 16.4 across the 14 cluster sample. Although the distances to the clusters range from 1.0 to 6.2 kpc ([Hoq & Clemens 2015](#)), all stars in each field were tested for *Gaia* matches and other selection effects. The same quality criteria were applied as for stars in the RW survey ( $m_H \leq 13$  mag and  $p/\sigma_p \geq 2$ ). In total, 893 stars from the 14 selected clusters met all selection and *Gaia*-match criteria and were used in the analysis.

### 2.3.4. Data handling and cross-match with Gaia

We cross-matched the Mimir polarization catalogs (RW survey and Open cluster surveys) with *Gaia* DR3 using a search radius of 1 arcsec. For the 12 sources that returned multiple matches, we selected the brightest source among the matches. The final catalog from the Mimir data contains 1371 unique sources with *Gaia* matches. To obtain stellar distances, we use the latest *Gaia*-based catalog providing probabilistic distance estimates based on parallax measurements ([Bailer-Jones et al. 2021](#)). We cross-matched our catalog with that of [Bailer-Jones et al. \(2021\)](#) based on the *Gaia* source identifier (which is the same for EDR3 and DR3). Throughout this work, we use the photo-geometric distance estimates from the [Bailer-Jones et al. \(2021\)](#) catalog. The P2025

catalog provides *Gaia* EDR3 matches and stellar distances from [Bailer-Jones et al. \(2021\)](#).

We convert the polarization angles  $\chi$  measured in the celestial frame (according to the IAU convention, increasing from north to the east) to angles in the Galactic reference frame,  $\theta$ , through (e.g., [Appenzeller 1968](#))

$$\theta = \chi + \arctan\left(\frac{\sin(l_{NCP} - l)}{\tan b_{NCP} \cos b - \sin b \cos(l_{NCP} - l)}\right), \quad (5)$$

where  $l_{NCP}, b_{NCP}$  are the Galactic longitude and latitude of the north celestial pole and  $l, b$  are the Galactic coordinates of each star.

## 3. Methods

We aim to determine whether the Galactic magnetic field geometry shows a disturbance associated with the undulating pattern seen in the dust structure that defines the RW. We use stellar polarization to trace the morphology of the magnetic field as projected on the sky. By selecting stars whose light is primarily extinguished and polarized by the RW, we can probe the plane-of-sky component of the magnetic field that aligns dust grains in the RW.

The flow dynamics leading to the existing undulating morphology of the RW likely have disturbed the magnetic field. To reject the hypothesis that the magnetic field is parallel to the mid-plane over the extent of the RW, we would need to detect a region with a magnetic field orientation that significantly departs from plane-parallel. We focus our analysis on the nearest portion of the RW. This choice simplifies the analysis of the magnetic field in two ways. First, it lifts the need for tomographic decomposition to trace the magnetic field, as would be needed if multiple components along the LOS contributed to the stellar polarization signal. If the RW is the first polarizing screen along the LOS, then we can simply trace its magnetic field by measuring the

polarization of stars immediately behind it. Second, the analysis of Heiles (1996) shows that the starlight polarization fraction is greater in the longitude range of interest, compared to other directions along the Local Arm. This implies that polarization in this area will be more easily detected.

### 3.1. Region of nearest approach

The RW spans a large range in Galactic longitude and distances from the Sun, while remaining within a smaller range of latitude, as shown in Fig. 1. We define the region for our study as the portion of the RW within distance  $d_{RW} < 300$  pc from the Sun. This distance cut corresponds to longitudes  $l = [122^\circ, 188^\circ]$ . We additionally impose a latitude cut of  $|b| < 25^\circ$ , and restrict our analysis to sightlines within  $10^\circ$  of the RW spine, encompassing the bulk of the extinction integrated along the LOS out to the limits of the Edenhofer et al. (2024) map. We present the spine of the RW in the longitude-distance plane in Fig. 2 (left). Stars in our catalogs are shown as dots in the figure, with different colors specifying the different surveys. The purple region marked on the spine of the RW denotes the longitude range where the RW is within 300 pc. We refer to this region of interest as the “nearest approach” – the area where the RW reaches its smallest distance from the Sun. Within this longitude range, the RW appears to cross the Galactic midplane ( $b = 0^\circ$ ) forming an angle of  $\sim 30^\circ$  with respect to the ( $b = 0^\circ$ ) line near  $l = 164^\circ$  (Fig. 1). Similarly to the best-fit model, the alternative spine models form angles of  $25\text{--}34^\circ$  with the midplane.

We calculate the angle between the tangent to the RW spine at point  $i$  and the plane of the sky,  $\gamma_i$ , for each location along the RW. The RW spine in the nearest approach region lies mostly in the plane of the sky, with  $\cos^2(\gamma_i) > 0.6$ . The linear extent of the RW model within this longitude range is 350 pc (the separation between the two end-points within the nearest approach region, measured in cartesian coordinates). The height (vertical to the disk, assumed to be at  $z = 0$ ) difference between the two end-points of the model in this region is 160 pc.

### 3.2. Star sample selection

We wish to select stars whose polarization is primarily due to the RW. Since there is no prior information on the polarization properties of the RW, we investigate the 3D distribution of extinction of the structure. If the extinction toward a star is dominated by dust associated with the RW, then it is likely that the star’s polarization too will be dominated by the RW (as long as the magnetic field is not directed along the LOS, in which case negligible polarization would arise).

We construct a map of the extinction in the distance-longitude plane. Because the range of latitudes is much smaller than the range of longitudes spanned by the RW (Fig. 1), collapsing along the latitude axis still allows us to view the two main axes of the object ( $l, d$ ) and provides a simple way to visualize the dust distribution along the lines of sight toward the RW. Since we are interested in visualizing the bulk of the extinction, we downgrade the resolution of each HEALPix map to  $N_{\text{side}} = 64$ . For all sky pixels within  $10^\circ$  of the RW we extract profiles of the differential extinction as a function of distance using the 3D dust map of Edenhofer et al. (2024). We now have independent profiles of differential extinction as a function of distance for the aforementioned sightlines. Since the differential extinction data are sampled on an irregular distance grid, we interpolate each profile to obtain a re-gridded profile sampled at regular distance intervals spaced by 1 pc, the approximate resolution of the

Edenhofer et al. (2024) map within a few hundred parsecs of the Sun. We create a coarse longitude grid with  $3^\circ$  spacing. Next, we construct a 2D map of extinction in the longitude-distance plane by summing the profiles of all sightlines within a given longitude bin at each distance. This results in a map of the total extinction as viewed along the latitude axis (spanning the selected latitudes and perpendicular to the longitude-distance plane).

This 2D extinction map is shown in Fig. 2 (right). The distribution of  $A_V$  shows overdensities that trace the RW model<sup>3</sup> (black line) for the extent of the RW at longitudes  $l \lesssim 150^\circ$ . Toward  $l = 160^\circ\text{--}185^\circ$  there is an offset between the peak of the dust distribution and the RW model. This longitude range encompasses the Taurus Molecular Cloud (TMC). There is also a notable absence of dust along the RW model for longitudes  $l > 215^\circ$ , beyond the Orion Molecular Cloud (at 0.45 kpc distance). The RW model was constructed by fitting a damped sinusoid function to the locations of discrete molecular clouds (Alves et al. 2020). Consequently, the fact that we do not find the model able to match all of the details of the 3D dust distribution is not surprising. For our purposes, it appears that this model is an adequate description of the large-scale geometry of the dust distribution.

Dust associated with the RW appears to provide the bulk of the extinction for most of our selected sightlines out to the boundaries of the 3D map. However, this is not the case in the longitude range  $l \in [100^\circ, 170^\circ]$ , where dust reddening shows overdensities at distances  $> 400$  pc that do not appear to be part of the RW (the differential reddening drops to zero in between the RW and those structures). To be conservative, we conclude that the extinction of stars at distances between the RW and 400 pc, within the longitude range  $l \in [122^\circ, 188^\circ]$  and within the sky area of  $10^\circ$  from the RW spine, is dominated by the dust associated with the RW. This also suggests that the polarization of those stars will be dominated by the RW, barring 3D magnetic field geometry effects (inclination, LOS tangling within the RW itself that may cause depolarization).

In the following, we distinguish between two stellar samples occupying the same region on the sky (within  $10^\circ$  of the RW spine, having  $l = [122^\circ, 188^\circ]$  and  $|b| < 25^\circ$ ). The “far” sample corresponds to stars with distances beyond 1.2 kpc ( $d > 1.2$  kpc). We define our default near sample to include stars with distances  $d < 400$  pc. In Sect. 4, we incrementally increase this distance limit to create near samples out to 1.2 kpc. We place a S/N threshold in polarization fraction:  $p/\sigma_p \geq 2.5$ , which corresponds to an uncertainty in the polarization angle of  $\leq 12^\circ$ . The main effect of this S/N threshold is to remove stars that are foreground to the RW, where there is too little dust to induce measurable polarization above our survey sensitivity limits.

A final selection cut is implemented to remove stars toward the TMC. The magnetic field in this cloud may not trace the large-scale magnetic field of the RW. In the TMC, the magnetic field has been perturbed by a nearby supernova explosion, forming the so-called “Per-Tau” shell, as well as by other smaller-scale feedback events (see, e.g., Chapman et al. 2011; Bialy et al. 2021; Doi et al. 2021; Soler et al. 2023; Konietzka et al. 2024). The cloud appears to be squeezed between the Per-Tau shell and the Local bubble (Zucker et al. 2022). We define a circular region centered on  $(l, b) = (172.6^\circ, -15.6^\circ)$ , following Table 1 of Zucker et al. (2021). We chose a radius of  $10^\circ$ , which encompasses the entire length of the TMC as found in that work and removed all stars in our sample within that area.

<sup>3</sup> Hereafter, ‘RW model’ refers to the default model unless otherwise specified.

### 3.3. Producing pixelized stellar polarization data

Our aim is to compare the mean orientation of the GMF with that of the RW on scales larger than those of individual clouds (i.e.,  $\sim 5$ – $10$  pc, Zucker et al. 2021). At the nearest distance to the RW of 300 pc, these scales correspond to angular separations of 1–2 degrees. We therefore wish to homogenize the sampling over the entire sky area of interest to these scales. The sightlines toward stars with measured polarization are unevenly spaced on the sky. For example, the fields observed with Mimir toward the RW may contain tens of stars at all distances within the  $10' \times 10'$  field of view. By averaging the stellar polarization data over degree-sized scales we avoid overweighting sky pixels with many stellar measurements as a result of the observing strategy.

We pixelize the stellar polarization angles to  $N_{\text{side}} = 64$ . Within each pixel, we calculate the weighted mean polarization angle,  $\theta^*$ , of the  $N$  stars within the pixel weighting by their inverse variances

$$\theta^* = \frac{1}{2} \arctan(\bar{u}, \bar{q}), \quad (6)$$

as appropriate for circular data (e.g., Fisher 1995), where we use the two-argument arctangent function. The quantities  $\bar{u}, \bar{q}$  are

$$\bar{q} = \frac{1}{W} \sum_{i=1}^N w_i \cos(2\theta_i), \quad (7)$$

$$\bar{u} = \frac{1}{W} \sum_{i=1}^N w_i \sin(2\theta_i), \quad (8)$$

where  $W$  is the sum of the weights,  $w_i$ , with  $w_i = (\sigma_{\theta_i})^{-2}$  and  $W = \sum_{i=1}^N w_i$ . We wrap all resulting angles to the range  $[0, \pi]$ . We compute the error on the weighted mean quantity  $\bar{q}$  (and similarly for  $\bar{u}$ ) according to the second method presented in Gatz & Smith (1995) as

$$\sigma_{\bar{q}} = \sqrt{\frac{N}{(N-1) \sum_{i=1}^N w_i^2} [A + B + C]}, \quad (9)$$

where

$$A = \sum_{i=1}^N (w_i q_i - \bar{w}_i \bar{q}_i)^2, \quad (10)$$

$$B = 2\bar{q}_i \sum_{i=1}^N [(w_i - \bar{w}_i)(w_i q_i - \bar{w}_i \bar{q}_i)], \quad (11)$$

$$C = \bar{q}_i^2 \sum_{i=1}^N (w_i - \bar{w}_i)^2, \quad (12)$$

where  $\bar{w}_i$  is the mean weight and  $q_i = w_i \cos(2\theta_i)$ .

As a result of inhomogeneous observing strategies, and the presence of star clusters in some fields, some pixels have a high number of stars. The weighted mean orientation in such pixels can have an uncertainty of less than  $1^\circ$ . However, the systematic uncertainty in the calibration of the polarization angle of stars is  $\sim 1^\circ$  (Clemens et al. 2012; Blinov et al. 2023). To avoid underestimating the total uncertainty of the polarization angle, we restrict the minimum uncertainty of the polarization angle in any pixel to  $\sigma_\theta = 1^\circ$ . We have checked that changing this lower limit from  $0.5^\circ$ – $2^\circ$  does not affect the results of the mean relative orientation of stellar polarization with respect to the RW.

### 3.4. Statistics of angles

In this work we wish to compare the polarization angle of stars to the projected shape of the RW on the plane of the sky. We quantify the significance of the alignment between two sets of angles with the Projected Rayleigh Statistic (PRS, Jow et al. 2018). The PRS is a measure of the narrowness of a distribution of angle differences. Values close to zero imply a random distribution. Values that are highly positive (negative) imply alignment (orthogonality). We compute the PRS, symbolized by  $V$ , taking into account measurement uncertainties, as:

$$V = \frac{1}{\sqrt{\sum_{i=1}^N w_i^2 / 2}} \sum_{i=1}^N w_i \cos 2\Delta\psi_i, \quad (13)$$

where  $\Delta\psi_i$  is the difference between two angles and  $w_i$  is the weight as defined for Eq. (6).

As defined in Eq. (13), the value of the PRS depends on the number of measurements. To be able to reliably compare the PRS among datasets with different numbers of measurements, we normalize the PRS by its maximum possible value,  $V_{\text{max}}$  (i.e., Eq. (13)) when all angles are zero:

$$\frac{V}{V_{\text{max}}} = \frac{V}{\frac{1}{\sqrt{\sum_{i=1}^N w_i^2 / 2}} \sum_{i=1}^N w_i}. \quad (14)$$

In Sect. 4, we compare the normalized PRS,  $V/V_{\text{max}}$ , for a set of angles of interest, to that of a uniform distribution of angle differences to quantify the significance of the alignment (Jow et al. 2018).

## 4. Results

### 4.1. Magnetic field orientations toward the Radcliffe wave

In Fig. 3, we compare the polarization angles of dust emission at 353 GHz from *Planck* (after rotation by  $90^\circ$ ) with stars in the default near sample (stellar distances  $d < 400$  pc). We show the *Planck* polarization data as segments (light brown lines), where the tilt of the segment corresponds to the angle  $\theta_{\text{dust}}$  at that pixel, while the segment length is the same for all pixels. For ease of visualization, we show the *Planck* data at  $N_{\text{side}} = 32$ , while we use  $N_{\text{side}} = 64$  for the quantitative analysis. Each yellow line segment represents the mean polarization angle of stars in that pixel. The cyan line shows the projection of the RW model on the sky in this area, while the background image is the extinction out to 400 pc, encompassing the bulk of the extinction from the RW in the nearest-approach region.

We observe a difference between these two tracers of the magnetic field. The *Planck* data show a mean orientation of the magnetic field of  $-88^\circ$ ; essentially parallel to the midplane of the Galaxy. The only significant local deviation is seen toward the TMC. The magnetic field there is known to be dominated by the TMC, and starlight polarization is well-aligned with the magnetic field traced by polarized dust emission (Soler et al. 2016). In contrast to the dust emission, the magnetic field as traced by stars within  $d < 400$  pc shows an offset with respect to the midplane, most notably around longitude  $l = 165^\circ$ .

We quantify this offset between the mean orientation traced by stars and by the dust emission as follows. We construct pixelized maps of the stellar polarization angles at  $N_{\text{side}} = 64$  (resolution approximately  $1^\circ$ ) including stars within 400 pc (see

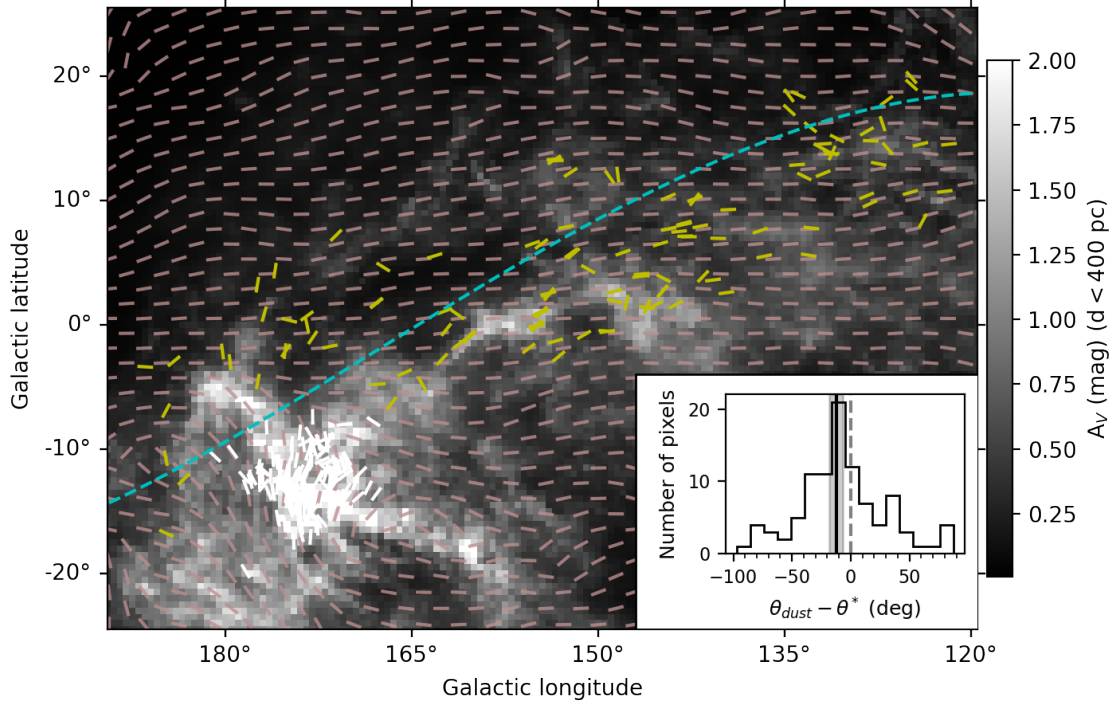


**Fig. 3.** Comparison between the pixelated polarization angles of stars and those of dust emission in the nearest approach region of the RW to the Sun. The polarization angles of stars with significant polarization fraction, within 400 pc from the Sun and within 10 degrees angular separation of the RW are shown as yellow segments. White segments show the stars excluded from the analysis due to their projected proximity to the TMC. Light brown segments show the orientation of the plane-of-sky magnetic field derived by rotating the *Planck* 353 GHz data by 90 degrees. The cyan dashed line shows the spine of the RW as projected on the sky, while the background image shows the extinction out to 400 pc. The inset on the bottom right shows the distribution of angle differences between the *Planck*-inferred magnetic field orientation and the polarization angles of stars at  $N_{\text{side}} = 64$  excluding sightlines toward the TMC. The circular mean and its error are shown as a vertical black line and a gray band. The dashed vertical gray line in the inset indicates a relative orientation of  $0^\circ$ .

Sect. 3). We select pixels where the polarization angle uncertainty is  $<12^\circ$  (corresponding to an S/N cut in polarization of 2.5), both in the *Planck* map and in the stellar polarization map. This selection cut on the stellar polarization S/N only removes 2 of the 164 pixels, while 85% of the pixels have uncertainties in the mean polarization angle of less than  $5^\circ$ . The *Planck* polarization data that remain are highly significant, with all pixels having  $S/N > 8$ . We exclude stars near the TMC. The distribution of angle differences between the *Planck*  $\theta_{\text{dust}}$  and the pixelized stellar polarization angles  $\theta^*$  is shown in the inset of Fig. 3. We observe that the distribution is offset from  $0^\circ$ . The weighted circular mean of the distribution is  $-13^\circ \pm 6^\circ$ . This offset reflects a shift in the mean orientation of the magnetic field as traced by the stars compared to the dust emission. The standard deviation of the distribution of angle differences is  $38^\circ$ , much larger than the uncertainties of the mean polarization angle in individual pixels ( $\sim 1^\circ$ ). These differences may arise from line-of-sight integration effects: dust unrelated to the RW exists at distances beyond 400 pc (Fig. 2), and likely contributes to the polarization of the dust emission traced by *Planck*.

To investigate whether this offset occurs at a specific distance, we compare the stellar data within 400 pc to the far sample (beyond 1.2 kpc). We construct maps of the weighted mean polarization angle within pixels of  $N_{\text{side}} = 64$ , using the equations described in Sect. 3 and show them in Fig. 4. Data from stars in the near sample are shown in the left panel and data from stars in the far sample are shown in the right panel. At each pixel location, we show a yellow line segment representing the mean Galactic polarization angle of stars in that pixel. Sightlines toward the TMC are excluded from both samples –

we show their corresponding Galactic polarization angles with white lines.

In Fig. 4, the orientations of the stellar polarization measurements of the near sample show significant offsets from those of the far stars. The polarization angles of the far sample star pixels are more aligned with the Galactic midplane, in agreement with the *Planck* data. In contrast, the orientations of the magnetic field traced by nearby stars appear to be aligned with the projected position angle of the RW model (cyan line).

We quantify the relative orientations between the RW model and the stellar polarization data as follows. For each pixel in the binned star polarization map, we find the nearest (in projection) position of the RW model. We calculate the projected position angle of the model at that location ( $\psi_{\text{RW}}$ ). Then, we compute the angle difference between the mean star polarization angle in the pixel and  $\psi_{\text{RW}}$ .

Figure 5 shows histograms of the relative orientations between the binned stellar polarization angles and the default RW model for the two aforementioned samples: stars in the near sample out to 400 pc (panel A) and stars in the far sample (panel B). The near sample distribution has a weighted circular mean of  $4^\circ \pm 4^\circ$ <sup>4</sup>. The mean orientation of the polarization of these stars is consistent with alignment with the RW shape. In contrast, the far star sample distribution has a circular mean of  $24^\circ \pm 1^\circ$ , significantly offset from alignment with the RW.

We also compare the polarization angles of star pixels with respect to the midplane of the Galaxy in the bottom panels of

<sup>4</sup> For all angle difference distributions, we computed the error on the mean via the equations presented in Section 3.3.

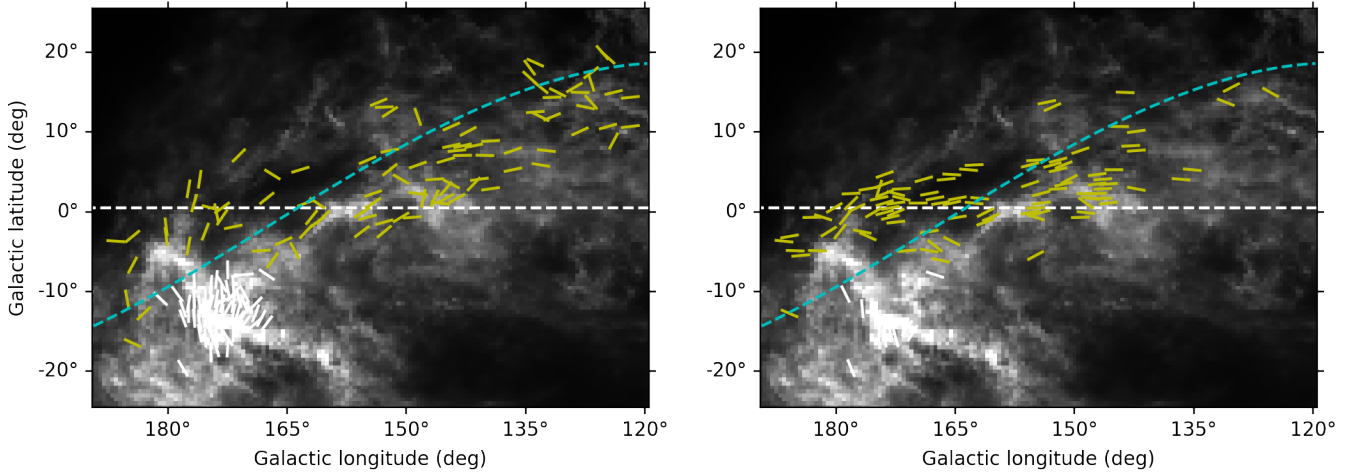


**Fig. 4.** Comparison between pixelized star polarization angle maps for stars within 400 pc (left) and stars beyond 1.2 kpc (right). Each yellow line segment traces the mean polarization angle of stars in a given pixel. The polarization angles of pixels toward the TMC (white segments) are excluded from the analysis. The Galactic plane is marked with a white horizontal dashed line. The background image shows the cumulative extinction out to 400 pc from [Edenhofer et al. \(2024\)](#) (as in Fig. 3).

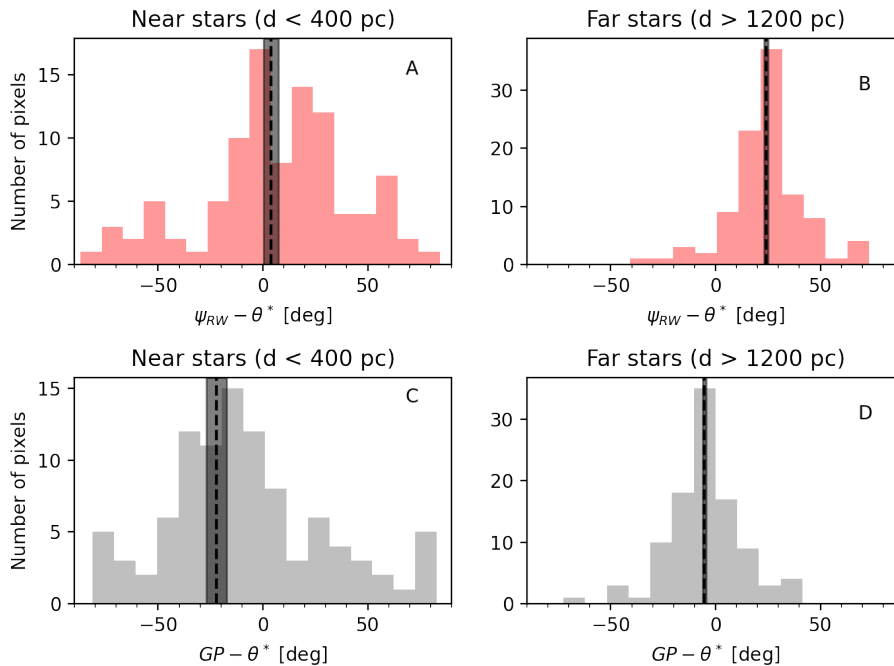


**Fig. 5.** Relative orientations of pixelized star polarization angles and the position angle of the RW (red, top row) or the Galactic midplane (gray, bottom row). Panels A and C show distributions for stars within 400 pc, while panels B and D those for stars beyond 1.2 kpc. The vertical gray band in each panel is centered on the circular mean of each distribution (dashed vertical line) and has a width equal to two times the uncertainty on that mean.

**Fig. 5.** In this case, the far sample (panel D) shows a circular mean much closer to alignment:  $-5^\circ \pm 1^\circ$ . The distribution of relative orientations for the near sample with respect to the midplane (panel C) has a circular mean of  $-20^\circ \pm 5^\circ$ , inconsistent with midplane alignment.

We conclude that the near stars trace a plane of sky magnetic field that is aligned with the projected shape of the RW. In contrast, the far stars show polarization angles that are well aligned with the direction of the Galactic midplane.

The spread of the distribution of relative orientations also changes dramatically when considering the near vs. far samples. The standard deviation of the distribution of relative orientations for nearby stars with respect to the RW is  $35^\circ$ . The far sample

has a standard deviation of  $17^\circ$ . These values do not change appreciably between the midplane and RW comparisons.

One possible reason for the narrower spread in the distribution of angle differences for the far stars is that we are probing the magnetic field averaged over larger volumes. The linear size of the RW within the nearest approach region is 350 pc, while the minimum separation between pixels of  $1^\circ$  corresponds to 5 pc (taking the bulk of the dust to lie at a distance of 300 pc, Fig. 2). The far stars trace the cumulative Stokes parameters out to large distances and therefore may exhibit less scatter due to averaging along the line of sight. In addition, as a result of our observing strategy, we have multiple far stars in each field of view. Therefore, star measurements are averaged in the plane of

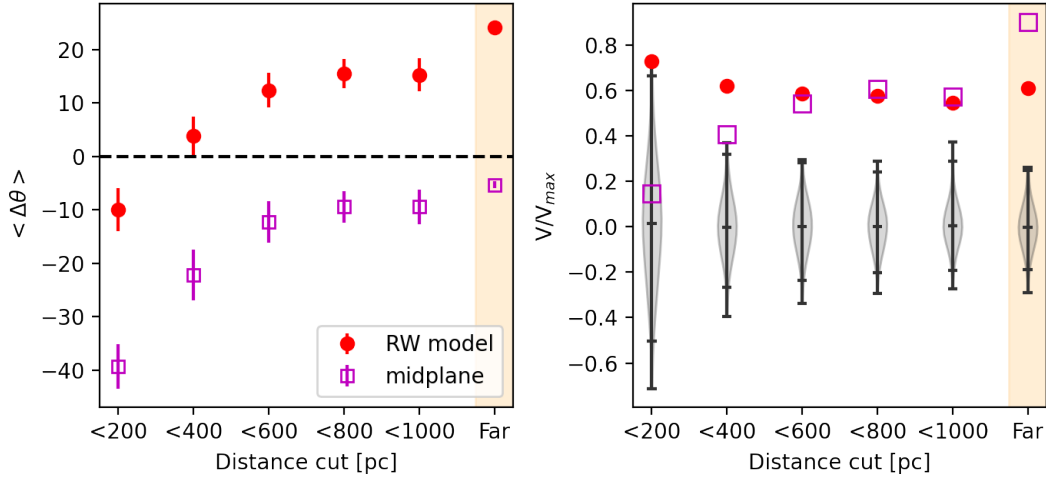


**Fig. 6.** Comparison of alignment and alignment significance as a function of the maximum distance of stars. Left: circular means ( $\langle \Delta\theta \rangle$ ). Right: normalized PRS ( $V/V_{max}$ ). Each panel shows values of these quantities computed for (a) the relative orientation of star polarization angles compared to the RW (red circles), (b) the relative orientation with respect to the midplane (magenta squares). The violin shapes show the distribution of normalized PRS values obtained for a uniform distribution of angles for the same uncertainties as the corresponding stellar samples. Horizontal lines mark the median, three-sigma lower and upper limits and the minimum and maximum value of each distribution.

the sky during the pixelization process. For a distance of 3 kpc, stars averaged over  $1^\circ$  pixels are tracing a magnetic field averaged over 50 pc projected linear size. In short, averaging both along the line of sight and across the plane of the sky for the far sample is likely the main reason for the much reduced scatter of the distributions of relative orientations for the far stars.

#### 4.2. Quantifying the relative orientations as a function of distance

In the previous section, we have shown that the polarization angles of stars closer than 400 pc differ substantially from those of stars in the far sample. We have also shown that the distribution of relative orientations of starlight polarization within 400 pc compared to the RW model peaks at  $\approx 0^\circ$ , consistent with an alignment of the magnetic field traced by nearby stars with the shape of the RW as projected on the sky. In this section, we quantify the significance of this alignment between the magnetic field and the RW as a function of stellar distance.

We construct samples of stars with different maximum distances, starting from 200 pc and incrementally increasing the maximum distance of the stars by 200 pc to a maximum of 1 kpc. The far sample remains as defined originally (minimum distance of 1.2 kpc).

To quantify the alignment between two sets of angles, we use two measures: (i) the circular mean of the distribution of relative orientations and (ii) the normalized PRS. The former quantifies the proximity of the mean relative orientation to zero (indicating alignment), while the latter quantifies the significance of that alignment compared to a uniform distribution (a measure of the spread of the distribution of relative orientations). We expect a significant alignment to manifest as both a near-zero mean relative orientation and a high normalized PRS (significant compared to a uniform distribution).

Figure 6 (left) shows the circular mean of the distribution of relative orientations,  $\langle \Delta\theta \rangle$ , of pixelated stellar polarization with respect to the RW model (red circles) and with respect to the Galactic plane (open square symbols), as a function of the maximum distance cut. The first sample extending out to 200 pc shows an offset of  $\sim 10^\circ$  from the RW orientation. This sample

has the smallest number of pixels. As the maximum distance is increased, and the number of stars sampled increases, the error on the circular mean decreases. The samples out to 400 pc show a mean relative orientation with respect to the RW consistent with alignment within  $1\sigma$ . From the sample with  $<600$  pc onward, we observe a non-negligible offset between the stellar polarization orientations and those of the RW (red circles). The largest offset with respect to the RW is seen for the far sample (right-most red circle).

At the same time, the mean relative orientation of starlight polarizations compared to the Galactic plane is never consistent with  $0^\circ$ . The far star sample has a mean orientation with the smallest offset compared to the Galactic plane of  $-7^\circ$  (open square symbols). We conclude that for stars out to 400 pc, the polarizations are on average well-aligned with the RW, while this is not the case for alignment with the midplane direction.

Next, we quantify the significance of the alignment discussed above. For each pixelized star sample, we compute the normalized PRS (Eq. (14)) and compare it to the normalized PRS of a uniform distribution. We randomize the relative orientation angles by drawing values from a random uniform distribution in the range  $[-90^\circ, 90^\circ]$ . For each measurement, we sample an ‘observation’ by drawing from a Normal distribution centered on the random value obtained from the uniform distribution, with a standard deviation equal to the corresponding uncertainty in the measured polarization angle of the pixel. We repeat the generation of a set of random angles for each near and far sample 2000 times and compute the PRS each time.

Figure 6 (right) shows the normalized PRS for the distributions of relative orientations at each distance limit: (a) the pixelized stellar polarization versus RW position angle ( $\psi_{RW} - \theta^*$ , red circles), (b) the pixelized stellar polarization versus midplane direction ( $GP - \theta^*$ , purple squares), and (c) the case of a randomized distribution of angle differences (violin shapes).

We find that the alignment with the RW seen for the near star sample  $d < 400$  pc is significant: the normalized PRS is greater than the values obtained from the randomized distributions. For samples with  $d < 600$  pc or larger, though the PRS of the  $\psi_{RW} - \theta^*$  distributions are significant, the circular means are not consistent with alignment with the RW.

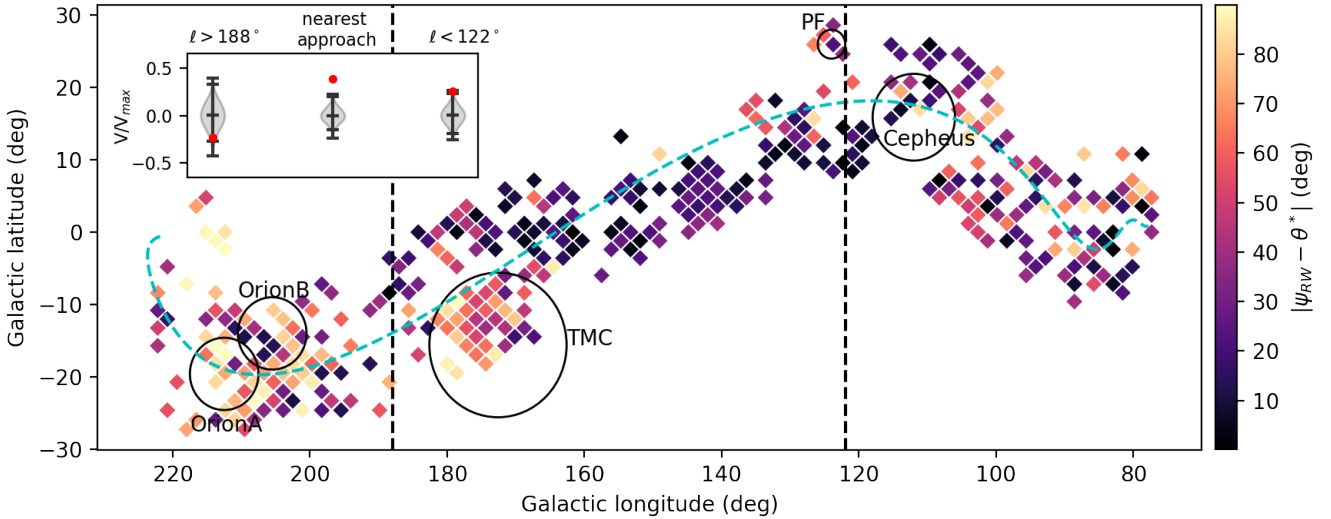


**Fig. 7.** Map of angle differences between the RW spine and pixelized stellar polarization angles. This covers the entire extent of the RW, for stars with distances  $< 1.2$  kpc. The molecular clouds annotated are: TMC, Orion A, Orion B, Cepheus, and the Polaris Flare (PF). Vertical dashed lines mark the nearest approach region within  $l = (122^\circ, 188^\circ)$ . The inset shows the normalized PRS for the three longitude ranges indicated in the main panel ( $l > 188^\circ$ , the nearest approach range, and  $l < 122^\circ$ ). For an explanation of the violin plots and red markers see Fig. 6.

The offset between the RW shape and the stars beyond 600 pc may result from the presence of dust structures unassociated with the RW, some of which can be seen in Fig. 2 (right). The far sample shows a highly significant PRS of the GP  $-\theta^*$ , and a small offset of the mean from  $0^\circ$ , indicating that the far stars are more well-aligned with the midplane than with the RW, as seen initially in Fig. 4.

#### 4.3. Relative orientations spanning the entirety of the RW

In the previous sections, we focused on tracing the magnetic field of the RW at its nearest approach to the Sun. We showed that the RW magnetic field is not consistent with lying along the midplane of the Galaxy. Instead, the magnetic field appears to be aligned with the shape of the RW spine in projection. The next question pursued is whether this apparent alignment holds throughout the full extent of the RW.

In Fig. 7, we show the absolute relative orientations between the position angle of the RW and the pixelated stellar polarizations. The data used here include stars out to 1.2 kpc, the maximum distance of the RW. The stellar data have again been pixelized to  $N_{\text{side}} = 32$  for better visualization, but the results are consistent with those at  $N_{\text{side}} = 64$ . We only show pixels with uncertainty in angle differences  $< 12^\circ$ . It appears that alignment over multiple adjacent pixels is only observed within the range of longitudes of the RW nearest approach ( $l = 122^\circ - 188^\circ$ ).

To quantify the degree of alignment of the RW magnetic field with the RW shape, we separate the data shown in Fig. 7 into three longitude ranges: the range of the RW nearest approach, the range of RW longitudes  $l > 188^\circ$ , and that with  $l < 122^\circ$ . In the inset of Fig. 7, we show the normalized PRS for the three longitude ranges, with symbols as in Fig. 6. As can be seen from comparing with Fig. 2, the RW is oriented mostly along the LOS in the two extreme longitude ranges, and mostly along the plane-of-sky in the middle one. We see that only the longitude range of nearest approach has a significant normalized PRS, while outside this range the PRS values are consistent with arising from random distributions. We speculate three possible reasons for this.

The first possibility is that the large-scale Galactic magnetic field is not aligned with the spine of the RW, with the exception

of the nearest approach region. The second possibility, is that local small-scale distortions of the magnetic field are dominating the observed polarization angles of the stars. We note that Fig. 7 and the corresponding PRS analysis includes stars tracing various molecular clouds that appear along the RW (notably, the TMC, Orion A and B as well as the Polaris Flare). We have annotated their locations and approximate sizes as circles in the figure. The central positions are taken from Zucker et al. (2021). For the Polaris Flare we used the center of the *Herschel* map (e.g., Panopoulou et al. 2016). The diameter of each circle corresponds to the projection of the maximum extent of the cloud's skeleton defined in Zucker et al. (2021). Feedback events, gravitational collapse and turbulence may have distorted the magnetic field from its initial configuration in such dense molecular clouds. The magnetic field around the Orion clouds is known to have been affected by the Orion-Eridanus superbubble (Soler et al. 2018). The third possibility is that the large-scale magnetic field is aligned with the RW in 3D, but the alignment is lost in projection as the structure moves away from the plane of sky and becomes increasingly parallel to the LOS. In this case we predict greater scatter in the polarization angles of the stars in the regions where the RW is pointing mostly along the LOS. Given the evidence in the literature that the magnetic field is parallel to the Local Arm in 3D (see Sect. 5), we favor the latter possibility. More detailed modeling of the RW magnetic field geometry is needed to distinguish among the above scenarios.

#### 4.4. Dependence on the choice of RW model

We repeat the analysis presented in Sects. 4.1, 4.2, and 4.3 for the 20 alternative models of the RW spine (Sect. 2) to investigate any dependence of the results on the choice of model. We find that the star sample within 400 pc is aligned with the RW for 13 of the 20 models. In three out of the 20 models the sample within 600 pc also shows alignment with the RW. Models that cross the midplane at longitude less than  $159^\circ$  have  $\langle \Delta\theta \rangle$  that are inconsistent with alignment. This indicates that the latter models do not provide a good description for the mean magnetic field in the RW.

The results of Figure 7 are robust to the choice of model. For all models the PRS in the nearest approach longitude range is significant, while that in the other two longitude ranges remains consistent with that from a random distribution of angles.

## 5. Discussion

We have performed a study of the polarization angles of stars toward the region of the sky where the RW is nearest to the Sun. We have determined that the polarization angles vary with distance in a systematic fashion. Stars within 400 pc of the RW trace a magnetic field that is aligned with the projected shape of the RW. In contrast, stars farther than 1.2 kpc have polarization angles that are preferentially aligned with the Galactic plane (Fig. 6).

We note that the observed polarization angles of stars correspond to the cumulative polarization tracing dusty structures out to the distance of each star. At the distance of nearest approach of the RW, the stellar polarization is dominated by dust in the RW itself, thus tracing the local-to-the-RW magnetic field orientation (Fig. 2). For distances beyond the RW, stellar polarization may arise from multiple components along the line of sight, similarly to what is found for polarized dust emission throughout the sky (e.g., Halal et al. 2024). A tomographic decomposition of the Stokes parameters with distance would be necessary to determine whether the magnetic field is aligned locally with the midplane at distances beyond the RW (Pavel 2014; Panopoulou et al. 2019; Pelgrims et al. 2023, 2024, Doi et al. 2024).

Previous analyses of stellar polarization toward the Local Arm found a mean polarization orientation parallel to the Galactic midplane (Fosalba et al. 2002), especially for stars farther than 1 kpc (Heiles 1996). In our study we find that the magnetic field shows a mean offset from the midplane of  $18^\circ$  over the nearest approach longitude range. At the longitude where the RW crosses the midplane, both the RW and the magnetic field form an angle of  $\sim 30^\circ$  with the plane. The linear size of the region within which the magnetic field departs from plane-parallel geometry is 350 pc.

Localized, smaller angular-scale deviations from a parallel to the midplane geometry have been noted toward other regions of the Galaxy (Pavel 2014; Versteeg et al. 2023; Doi et al. 2024). Clemens et al. (2020) pointed out that deviations from the Galactic midplane direction are relatively common when looking at the observed polarization angles of stars in their extensive H-band polarization survey toward the inner Galaxy. Determining whether the large-scale deviation found in the RW is an exception, or whether such deviations are more prevalent throughout the disk, would be essential for an accurate description of the large-scale GMF.

### 5.1. Implications for large-scale GMF modeling.

Determining the 3D geometry of the coherent component of the magnetic field in the Local Arm is necessary for constructing accurate models of the GMF. The RW traces only a 3 kpc section of the Local Arm, while the entire arm extends over 8 kpc as determined by maser observations (Reid et al. 2019).

Previous studies using stellar polarization or rotation measures of pulsars have shown that the coherent component of the magnetic field in the solar vicinity points toward longitude  $l = 70\text{--}95^\circ$  (Manchester 1974; Rand & Kulkarni 1989; Heiles 1996). Significant discrepancies were initially found between stellar polarization and rotation measures (Ellis & Axon 1978;

Inoue & Tabara 1981). However, later estimates of the local direction of the magnetic field in the dusty ISM confirm a longitude range of  $l = 72\text{--}85^\circ$  from stellar polarization, (Heiles 1996), and  $l = 70\text{--}77^\circ$  at high latitudes from polarized dust emission (Planck Collaboration Int. XLIV 2016; Pelgrims et al. 2020). This longitude range was known to correspond to the direction in which we observe the Local Arm end-on (e.g., Heiles 1996), and also corresponds to the end-point of the RW (Fig. 7).

These previous studies inferred that the magnetic field is aligned with the Local Arm – a conclusion which is also confirmed by Faraday rotation toward extragalactic sources (Hutschenreuter & Enßlin 2020). On the basis of stellar polarization data, the 3D orientation of the GMF in the Local Arm was determined by modeling the stellar polarization fractions as a function of longitude (Inoue & Tabara 1981; Heiles 1996). In Sect. 4, we investigated a complementary tracer of the 3D direction of the magnetic field: the relative orientation of polarization angles with respect to the RW as a function of longitude. If the magnetic field was aligned with the RW throughout its extent, we would qualitatively expect near-perfect alignment in projection in the region where the RW is observed entirely in the plane of the sky. Conversely, due to distortions of the magnetic field, we would expect a loss of alignment in the projected relative orientations for the directions in which the RW is viewed end-on. These expectations qualitatively match the observed relative orientations in Fig. 7. A more complete stellar sample and detailed modeling are needed to infer whether 3D alignment with the RW is the best-fit geometry of the large-scale magnetic field of the structure.

Current GMF models constrain the magnetic field geometry to lie along the spiral arms as determined by a model for the thermal electrons (Jansson & Farrar 2012; Jaffe 2019). The RW is the gas reservoir of the Local Arm in the solar vicinity, and its shape is found to deviate from traditional models of spiral arms (Zucker et al. 2023). Our observations provide insights into the magnetic field in the dusty, neutral phase of the ISM. If the magnetic field is indeed found to follow the RW perturbation in 3D, then GMF models must be updated to include this sinusoidal perturbation in the large-scale magnetic field. It would be interesting to determine whether other observed corrugations in the gaseous disk (e.g., Veena et al. 2021) also have a counterpart in the GMF geometry.

Finally, our constraints on the GMF geometry toward the RW have implications for the distance determination of a prominent feature in the radio sky known as the Fan region (Brouw & Spoelstra 1976). The distance to the Fan region remains unclear. Depolarization by distant ionized sources implies that 30–40% of the emission at 1.5 GHz arises from a distance larger than 2 kpc (Hill et al. 2017). However, recent modeling of the polarized synchrotron emission suggested a local origin, associated with the RW (West et al. 2021). The polarization angles of the synchrotron emission in the Fan region trace a magnetic field that is parallel to the midplane. Given our findings that the magnetic field is not parallel to the midplane at the distance of the RW, it is unlikely that the Fan region coincides with the RW as suggested by West et al. (2021). Our results, however, do not rule out the existence of a component of the cold, dusty ISM that coincides with the synchrotron emitting volume giving rise to the Fan region beyond the distance of the RW.

### 5.2. Implications for the formation mechanism of the RW

Three classes of models have been proposed to explain the formation of the RW. The first model proposes that the RW

arose from a perturbation of the Galactic disk by the passage of a dwarf Galaxy (Alves et al. 2020). This scenario addresses the fact that perturbations are observed in the kinematics of stars (Thulasidharan et al. 2022). A second scenario posits the observed undulation of the RW is the result of feedback events (e.g., multiple clustered supernovae at different locations along the RW, Alves et al. 2020). A third scenario is that the RW is the result of an instability inherent in the disk, such as a Kelvin-Helmholtz instability (Fleck 2020).

Our magnetic field observations provide additional constraints that any viable mechanism should satisfy. The magnetic field is ordered over lengthscales of 300–400 pc and exhibits an inclined crossing with respect to the midplane, at the location where the RW crosses the midplane. In projection, the magnetic field appears aligned with the RW spine. We hypothesize that the magnetic field is aligned in 3D with the RW, as suggested by our results in Fig. 7 and the previous discussion. It is possible that the aforementioned scenarios would predict different magnetic field geometries, for example depending on the level of turbulence they induce in the gas as a function of scale. Explicit predictions for the magnetic field from these types of formation mechanisms would require MHD simulations.

A potentially interesting consequence of the presence of a large-scale perturbation in the magnetic field is whether the Parker instability would be triggered (Parker 1966). If we hypothesize that the magnetic field lies parallel to the RW throughout its length, then the magnetic field would exhibit an oscillatory pattern, reminiscent of this instability. The spacing between peaks in the damped sinusoid model describing the RW spine is  $\sim 2$  kpc, comparable to the wavelength of the Parker instability parallel to the magnetic field (1–2 kpc, Heintz et al. 2020; Tharakkal et al. 2023). The structure of the magnetic field, which exhibits a coherent component over 350 pc (at least) and crosses the midplane is reminiscent of the antisymmetric mode observed in simulations of the Parker instability (Mouschovias et al. 2009). The timescale for the Parker instability to grow from a small perturbation is  $\sim 100$  Myr in solar neighborhood conditions (Heintz et al. 2020). However, the growth of the instability could be much faster for large perturbations (e.g., due to the passage of a spiral shock wave, Mouschovias et al. 1974). For example, Habegger et al. (2023) found that a point-like injection of a significant energy from cosmic-rays (from a cluster of supernovae explosions) can reshape the magnetic field and the ISM within a timescale as short as 20 Myr. If the passage of a dwarf galaxy has indeed caused an initial perturbation, it remains to be shown whether the instability would be excited in the disk.

The Parker instability has been difficult to robustly observe and it remains unclear whether it is suppressed in galaxies like the Milky Way (Kim & Ryu 2001; Kim et al. 2002; Tharakkal et al. 2023; Hopkins et al. 2024). While its signatures are suggested in the Faraday rotation patterns of nearby galaxies (Beck 2015), pinpointing its presence in the Galaxy has proven elusive. Observations of the instability in the Milky Way have been claimed in various works (Vrba 1977; Fukui et al. 2006; Sofue & Nakanishi 2017), but are hampered by confusion effects due to the unknown 3D geometry of the magnetic field. It has been suggested that the instability in conjunction with supernova feedback is responsible for the predominance of vertical H I filaments toward the inner Galaxy (Soler et al. 2022). If triggered by some initial perturbation related to the formation of the RW, the instability could grow to further affect the distribution of gas and magnetic fields in the structure over time. It would be interesting to investigate this possibility with MHD simulations.

## 6. Summary

We have carried out an investigation of the magnetic field geometry of the Radcliffe wave. We have combined archival stellar polarimetry with new NIR polarization measurements toward the nearest portion of the RW to trace the plane-of-sky component of the magnetic field.

We have shown that the RW is the main dust structure along the LOS for most sightlines within 1.2 kpc of the Sun (for sightlines within  $10^\circ$  of the RW spine). As a result, the observed polarization angles of stars immediately behind the RW appear to trace the magnetic field of this structure. By isolating stars within 400 pc of the Sun, we find a significant departure ( $20^\circ$ ) of the magnetic field from the midplane of the Galaxy. The plane-of-sky magnetic field appears aligned with the shape of the RW spine orientation within the longitude range  $l \in [122^\circ, 188^\circ]$ . In contrast, stars beyond 1.2 kpc have polarization angles preferentially aligned with the Galactic midplane, consistent with measurements of polarized dust emission by *Planck*.

We have investigated the significance of the observed alignment of stellar polarizations with the RW as a function of distance. We have shown that the alignment of the magnetic field with the RW is most significant for stars within 400 pc of the Sun.

We have compared the relative orientation of stellar polarization and the projected geometry of the RW over its entire extent. Significant alignment between the two geometries (in projection) is best found in the sky region where the RW is at nearest approach to the Sun. This observation is consistent with the magnetic field geometry being aligned with the RW in 3D. We have discussed the implications of our findings for Galactic magnetic field models as well as possible formation scenarios for the RW itself.

## Data availability

The data described in Section 2.3.2 is available at the CDS via anonymous ftp to [cdsarc.cds.unistra.fr](https://cdsarc.cds.unistra.fr) (130.79.128.5) or via <https://cdsarc.cds.unistra.fr/viz-bin/cat/J/A+A/694/A97>

*Acknowledgements.* We thank Ralf Konietzka for helpful discussions. The authors acknowledge Interstellar Institute’s program “II6” and the Paris-Saclay University’s Institut Pascal for hosting discussions that nourished the development of the ideas behind this work. This study was based on observations using the 1.8 m Perkins Telescope Observatory (PTO) in Arizona, owned and operated by Boston University. Data were obtained using the Mimir instrument, jointly developed at Boston University and Lowell Observatory and supported by NASA, NSF, and the W.M. Keck Foundation. This study was partially supported by grant AST 18-14531 from NSF/MPS to Boston University. VP acknowledges funding from a Marie Curie Action of the European Union (grant agreement No. 101107047). S.E.C. acknowledges support from the National Science Foundation under grant No. AST-2106607 and an Alfred P. Sloan Research Fellowship. JDS acknowledges funding from the European Research Council (ERC) via the Synergy Grant “ECOGAL – Understanding our Galactic ecosystem: From the disk of the Milky Way to the formation sites of stars and planets” (project ID 855130). JA acknowledges funding from the European Research Council (ERC) via the Advanced Grant “ISM-FLOW” (101055318). JBT acknowledges support from the DFG via SFB1491 “Cosmic Interacting Matters” (project no. 445052434). This work uses results from the European Space Agency (ESA) space mission *Gaia*. *Gaia* data are being processed by the *Gaia* Data Processing and Analysis Consortium (DPAC). Funding for the DPAC is provided by national institutions, in particular the institutions participating in the *Gaia* MultiLateral Agreement (MLA). The *Gaia* mission website is <https://www.cosmos.esa.int/gaia>. The work is based on observations obtained with *Planck* (<http://www.esa.int/Planck>), an ESA science mission with instruments and contributions directly funded by ESA Member States, NASA, and Canada. We make use of the HEALPix (Górski et al. 2005), astropy (Astropy Collaboration 2022), matplotlib (Hunter 2007), healpy (Zonca et al. 2019), and scipy (Virtanen et al. 2020) packages.

## References

- Alves, J., Zucker, C., Goodman, A. A., et al. 2020, *Nature*, **578**, 237
- Appenzeller, I. 1968, *ApJ*, **151**, 907
- Astropy Collaboration (Price-Whelan, A. M., et al.) 2022, *ApJ*, **935**, 167
- Bailer-Jones, C. A. L., Rybizki, J., Fouesneau, M., Demleitner, M., & Andrae, R. 2021, *AJ*, **161**, 147
- Beck, R. 2015, *A&A Rev.*, **24**, 4
- Beck, R., & Wielebinski, R. 2013, in *Planets, Stars and Stellar Systems*, 5: Galactic Structure and Stellar Populations, eds. T. D. Oswalt, & G. Gilmore, 641
- Bialy, S., Zucker, C., Goodman, A., et al. 2021, *ApJ*, **919**, L5
- Blinov, D., Maharana, S., Bouzelou, F., et al. 2023, *A&A*, **677**, A144
- Brouw, W. N., & Spoelstra, T. A. T. 1976, *A&AS*, **26**, 129
- Carrasco, J. M., Weiler, M., Jordi, C., et al. 2021, *A&A*, **652**, A86
- Chapman, N. L., Goldsmith, P. F., Pineda, J. L., et al. 2011, *ApJ*, **741**, 21
- Clark, S. E., Peek, J. E. G., & Putman, M. E. 2014, *ApJ*, **789**, 82
- Clark, S. E., Hill, J. C., Peek, J. E. G., Putman, M. E., & Babler, B. L. 2015, *Phys. Rev. Lett.*, **115**, 241302
- Clark, S. E., Peek, J. E. G., & Miville-Deschênes, M. A. 2019, *ApJ*, **874**, 171
- Clemens, D. P., Sarcia, D., Grabau, A., et al. 2007, *PASP*, **119**, 1385
- Clemens, D. P., Pinnick, A. F., & Pavel, M. D. 2012, *ApJS*, **200**, 20
- Clemens, D. P., Cashman, L. R., Cerny, C., et al. 2020, *ApJS*, **249**, 23
- Doi, Y., Hasegawa, T., Bastien, P., et al. 2021, *ApJ*, **914**, 122
- Doi, Y., Nakamura, K., Kawabata, K. S., et al. 2024, *ApJ*, **961**, 13
- Edenhofer, G., Zucker, C., Frank, P., et al. 2024, *A&A*, **685**, A82
- Ellis, R. S., & Axon, D. J. 1978, *Ap&SS*, **54**, 425
- Fisher, N. I. 1995, *Statistical Analysis of Circular Data* (Cambridge: Cambridge University Press)
- Fleck, R. 2020, *Nature*, **583**, E24
- Fosalba, P., Lazarian, A., Prunet, S., & Tauber, J. A. 2002, *ApJ*, **564**, 762
- Fukui, Y., Yamamoto, H., Fujishita, M., et al. 2006, *Science*, **314**, 106
- Gaia Collaboration (Prusti, T., et al.) 2016, *A&A*, **595**, A1
- Gatz, D. F., & Smith, L. 1995, *Atmos. Environ.*, **29**, 1185
- Górski, K. M., Hivon, E., Banday, A. J., et al. 2005, *ApJ*, **622**, 759
- Green, G. M., Schlafly, E., Zucker, C., Speagle, J. S., & Finkbeiner, D. 2019, *ApJ*, **887**, 93
- Habegger, R., Zweibel, E. G., & Wong, S. 2023, *ApJ*, **951**, 99
- Halal, G., Clark, S. E., & Tahani, M. 2024, *ApJ*, **973**, 54
- Han, J. L. 2017, *ARA&A*, **55**, 111
- Havorkorn, M. 2015, *Astrophysics and Space Science Library*, 407, Magnetic Fields in the Milky Way, eds. A. Lazarian, E. M. de Gouveia Dal Pino, & C. Melioli, 483
- Heiles, C. 1996, *ApJ*, **462**, 316
- Heiles, C. 2000, *AJ*, **119**, 923
- Heintz, E., Bustard, C., & Zweibel, E. G. 2020, *ApJ*, **891**, 157
- Hennebelle, P., & Inutsuka, S.-i. 2019, *Front. Astron. Space Sci.*, **6**, 5
- Hill, A. S., Landecker, T. L., Carretti, E., et al. 2017, *MNRAS*, **467**, 4631
- Hopkins, P. F., Squire, J., Su, K.-Y., et al. 2024, *Open J. Astrophys.*, **7**, 19
- Hoq, S. 2017, PhD thesis, Boston University, Massachusetts, USA
- Hoq, S., & Clemens, D. P. 2015, *AJ*, **150**, 135
- Hunter, J. D. 2007, *Comput. Sci. Eng.*, **9**, 90
- Hutschenreuter, S., & Enßlin, T. A. 2020, *A&A*, **633**, A150
- Inoue, M., & Tabara, H. 1981, *PASJ*, **33**, 603
- Jaffe, T. R. 2019, *Galaxies*, **7**, 52
- Jansson, R., & Farrar, G. R. 2012, *ApJ*, **757**, 14
- Jow, D. L., Hill, R., Scott, D., et al. 2018, *MNRAS*, **474**, 1018
- Kim, J., & Ryu, D. 2001, *ApJ*, **561**, L135
- Kim, W.-T., Ostriker, E. C., & Stone, J. M. 2002, *ApJ*, **581**, 1080
- Konietzka, R., Goodman, A. A., Zucker, C., et al. 2024, *Nature*, **628**, 62
- Lallement, R., Vergely, J. L., Babusiaux, C., & Cox, N. L. J. 2022, *A&A*, **661**, A147
- Li, G.-X., & Chen, B.-Q. 2022, *MNRAS*, **517**, L102
- Manchester, R. N. 1974, *ApJ*, **188**, 637
- Marchwinski, R. C., Pavel, M. D., & Clemens, D. P. 2012, *ApJ*, **755**, 130
- Mathewson, D. S., & Ford, V. L. 1970, *MmRAS*, **74**, 139
- Mouschovias, T. C., Shu, F. H., & Woodward, P. R. 1974, *A&A*, **33**, 73
- Mouschovias, T. C., Kunz, M. W., & Christie, D. A. 2009, *MNRAS*, **397**, 14
- Naghizadeh-Khouei, J., & Clarke, D. 1993, *A&A*, **274**, 968
- Panopoulou, G. V., Psaradaki, I., & Tassis, K. 2016, *MNRAS*, **462**, 1517
- Panopoulou, G. V., Tassis, K., Skalidis, R., et al. 2019, *ApJ*, **872**, 56
- Panopoulou, G. V., Markopouloti, L., Bouzelou, F., et al. 2025, *ApJS*, **276**, 15
- Parker, E. N. 1966, *ApJ*, **145**, 811
- Pavel, M. D. 2011, *ApJ*, **740**, 21
- Pavel, M. D. 2014, *AJ*, **148**, 49
- Pelgrims, V., Ferrière, K., Boulanger, F., Lallement, R., & Montier, L. 2020, *A&A*, **636**, A17
- Pelgrims, V., Panopoulou, G. V., Tassis, K., et al. 2023, *A&A*, **670**, A164
- Pelgrims, V., Mandarakas, N., Skalidis, R., et al. 2024, *A&A*, **684**, A162
- Planck Collaboration I. 2011, *A&A*, **536**, A1
- Planck Collaboration XII. 2020, *A&A*, **641**, A12
- Planck Collaboration IV. 2020, *A&A*, **641**, A4
- Planck Collaboration Int. XIX 2015, *A&A*, **576**, A104
- Planck Collaboration Int. XXI. 2015, *A&A*, **576**, A106
- Planck Collaboration Int. XXXII. 2016, *A&A*, **586**, A135
- Planck Collaboration Int. XXXV. 2016, *A&A*, **586**, A138
- Planck Collaboration Int. XLIV. 2016, *A&A*, **596**, A105
- Rand, R. J., & Kulkarni, S. R. 1989, *ApJ*, **343**, 760
- Reid, M. J., Menten, K. M., Brunthaler, A., et al. 2019, *ApJ*, **885**, 131
- Remazeilles, M., Delabrouille, J., & Cardoso, J.-F. 2011, *MNRAS*, **418**, 467
- Skrutskie, M. F., Cutri, R. M., Stiening, R., et al. 2006, *AJ*, **131**, 1163
- Sofue, Y., & Nakanishi, H. 2017, *MNRAS*, **464**, 783
- Soler, J. D., & Hennebelle, P. 2017, *A&A*, **607**, A2
- Soler, J. D., Alves, F., Boulanger, F., et al. 2016, *A&A*, **596**, A93
- Soler, J. D., Bracco, A., & Pon, A. 2018, *A&A*, **609**, L3
- Soler, J. D., Miville-Deschênes, M. A., Molinari, S., et al. 2022, *A&A*, **662**, A96
- Soler, J. D., Zucker, C., Peek, J. E. G., et al. 2023, *A&A*, **675**, A206
- Speagle, J. S. 2020, *MNRAS*, **493**, 3132
- Stephens, I. W., Looney, L. W., Dowell, C. D., Vaillancourt, J. E., & Tassis, K. 2011, *ApJ*, **728**, 99
- Swiggum, C., Alves, J., D'Onghia, E., et al. 2022, *A&A*, **664**, L13
- Tharakkal, D., Shukurov, A., Gent, F. A., et al. 2023, *MNRAS*, **525**, 5597
- Thulasidharan, L., D'Onghia, E., Poggio, E., et al. 2022, *A&A*, **660**, L12
- Tu, A. J., Zucker, C., Speagle, J. S., et al. 2022, *ApJ*, **936**, 57
- Vaillancourt, J. E. 2006, *PASP*, **118**, 1340
- Veena, V. S., Schilke, P., Sánchez-Monge, Á., et al. 2021, *ApJ*, **921**, L42
- Virtanen, P., Gommers, R., Oliphant, T. E., et al. 2020, *Nature Methods*, **17**, 261
- Versteeg, M. J. F., Magalhães, A. M., Havorkorn, M., et al. 2023, *AJ*, **165**, 87
- Vrba, F. J. 1977, *AJ*, **82**, 198
- West, J. L., Landecker, T. L., Gaensler, B. M., Jaffe, T., & Hill, A. S. 2021, *ApJ*, **923**, 58
- Xu, S., Ji, S., & Lazarian, A. 2019, *ApJ*, **878**, 157
- Zhang, X., Green, G. M., & Rix, H.-W. 2023, *MNRAS*, **524**, 1855
- Zonca, A., Singer, L., Lenz, D., et al. 2019, *J. Open Source Softw.*, **4**, 1298
- Zucker, C., Speagle, J. S., Schlafly, E. F., et al. 2019, *ApJ*, **879**, 125
- Zucker, C., Speagle, J. S., Schlafly, E. F., et al. 2020, *A&A*, **633**, A51
- Zucker, C., Goodman, A., Alves, J., et al. 2021, *ApJ*, **919**, 35
- Zucker, C., Goodman, A. A., Alves, J., et al. 2022, *Nature*, **601**, 334
- Zucker, C., Alves, J., Goodman, A., Meingast, S., & Galli, P. 2023, in *Astronomical Society of the Pacific Conference Series*, 534, Protostars and Planets VII, eds. S. Inutsuka, Y. Aikawa, T. Muto, K. Tomida, & M. Tamura, 43